PROCEEDINGS A

rspa.royalsocietypublishing.org

Research

CrossMark click for updates

Cite this article: Deng Y, Korvink JG. 2016 Topology optimization for three-dimensional electromagnetic waves using an edge element-based finite-element method. *Proc. R. Soc. A* **472**: 20150835. http://dx.doi.org/10.1098/rspa.2015.0835

Received: 9 December 2015
Accepted: 29 March 2016

Subject Areas:
computational physics, computer modelling and simulation, electromagnetism

Keywords:
topology optimization, three-dimensional, electromagnetic wave, divergence-free condition, edge element

Authors for correspondence:
Yongbo Deng
e-mail: dengyb@ciomp.ac.cn
Jan G. Korvink
e-mail: jan.korvink@kit.edu

Topology optimization for three-dimensional electromagnetic waves using an edge element-based finite-element method

Yongbo Deng[1] and Jan G. Korvink[2]

[1]State Key Laboratory of Applied Optics, Changchun Institute of Optics, Fine Mechanics and Physics (CIOMP), Chinese Academy of Sciences, Dongnanhu Road 3888, Changchun 130033, People's Republic of China
[2]Institute of Microstructure Technology, Karlsruhe Institute of Technology (KIT), Hermann-von-Helmholtzplatz 1, 76344 Eggenstein-Leopoldshafen, Germany

YD, 0000-0002-1237-040X

This paper develops a topology optimization procedure for three-dimensional electromagnetic waves with an edge element-based finite-element method. In contrast to the two-dimensional case, three-dimensional electromagnetic waves must include an additional divergence-free condition for the field variables. The edge element-based finite-element method is used to both discretize the wave equations and enforce the divergence-free condition. For wave propagation described in terms of the magnetic field in the widely used class of non-magnetic materials, the divergence-free condition is imposed on the magnetic field. This naturally leads to a nodal topology optimization method. When wave propagation is described using the electric field, the divergence-free condition must be imposed on the electric displacement. In this case, the material in the design domain is assumed to be piecewise homogeneous to impose the divergence-free condition on the electric field. This results in an element-wise topology optimization algorithm. The topology optimization problems are regularized using a Helmholtz filter and a threshold projection method and are analysed using a continuous adjoint method. In order to ensure the applicability of the filter in

THE ROYAL SOCIETY PUBLISHING

the element-wise topology optimization version, a regularization method is presented to project the nodal into an element-wise physical density variable.

1. Introduction

Current hot topics in electromagnetics and photonics research cover electromagnetic or photonic cloaking [1–4], surface plasmonic polaritons [5–8], metamaterials [9–12], metasurfaces [13,14] and band gap structure or photonic crystals [15], to name the most prominent. In these research areas, the control of electromagnetic or optical waves is realized by structures with complex spacial configurations using pre-selected materials, and the incident waves have complicated polarizations. Most of these situations cannot be reduced to two dimensions, except for a minority of cases involving linear polarized waves. For this complexity, physical intuition-based electromagnetic structure design has its limitations. To overcome these bounds, several inverse design tests have been implemented based on structural optimization methods [16–34], in which the method employed most is the topology optimization method. Topology optimization is currently regarded to be the most robust methodology for the inverse determination of material distribution in structures that meet given structural performance criteria. It was first developed for elastic material response by Bendsøe & Kikuchi [35], and then was extended to a variety of application areas, including acoustic, electromagnetic, fluidic and thermal problems [16,20–22,24–33,36–45], to list the most prominent. Most of the reports on topology optimization in electromagnetics have focused on applications, including beamsplitters [18,19], photonic crystals [16,17], cloaks [20–22], sensors and resonators [44,45], metamaterials [23–25], excitation of surface plasmons [26], and electromagnetic and optical antennas [27–29,34], without presenting the systemical topology optimization methodology for electromagnetic waves in three-dimensional space. Therefore, it is necessary to develop a unified and systematic topology optimization approach that sufficiently considers the physical complexity of three-dimensional electromagnetics.

It is, however, not straightforward to develop a finite-element-based topology optimization method for electromagnetic waves in three-dimensional space, because a divergence-free condition needs to be enforced. In the two-dimensional transverse electric or magnetic wave (TE or TM) cases, the divergence-free conditions ($\nabla \cdot \mathbf{D} = 0$ and $\nabla \cdot \mathbf{B} = 0$) are automatically satisfied when reducing the Maxwell equations to their associated Helmholtz equations, and the popular node element-based Galerkin finite-element method can be used to directly discretize the Helmholtz equations [46,47]. Being different from the two-dimensional case, a divergence-free condition is not automatically satisfied when solving three-dimensional electromagnetics with a node element-based Galerkin finite-element method, and results in spurious solutions. Two dominant approaches have been developed to enforce divergence-free conditions and eliminate the spurious solutions. The first approach is to add a penalty term of the least square form of the divergence-free condition to the weak form of the wave equation, and then to discretize the weak form with nodal elements. However, the use of a penalty term cannot eliminate the divergence of the solution completely, and also affects the solution accuracy [47]. The second approach is the use of edge elements, which assign degrees of freedom to the edges rather than to the nodes of the elements, in which a vector basis with inherent satisfaction of the divergence-free condition is used to implement the interpolation [46–49]. The edge elements have also removed the inconvenience of imposing boundary conditions at material interfaces, and the difficulty in treating conducting and dielectric edges and corners owing to field singularities [46,47]. Therefore, an edge element-based finite-element method is the more reasonable choice for discretizing the three-dimensional wave equations and for developing a topology optimization method for three-dimensional electromagnetic waves.

Previously, [23,24,34] have focused on three-dimensional topology optimization for electromagnetics based on the finite-element method. In [24,34], Diaz *et al.* and Erentok *et al.*

implemented the topology optimization of antennas and metamaterials without supplying sensitivity analysis details, which is important because of the additional divergence-free condition needed to be enforced by edge element-based instead of node element-based discretizition. In [23], Otomori *et al.* tested the level-set method-based topology optimization method for metamaterial design, by discretizing the three-dimensional wave equations with a node element-based finite-element method, which however does not uphold the divergence-free condition, so that their Galerkin-weighted variational formulation is not complete. We conclude that topology optimization for three-dimensional electromagnetics still requires methodological improvements before it can robustly cater for the needs of electromagnetic engineering. This paper focuses on addressing these issues.

Reports on topology optimization for electromagnetic waves are based on the density [30] and level-set method [31] for material interpolation. When compared with the density method, the drawbacks of the level-set method include a strong dependence on the initial guessed topology, a low-efficiency of convergence and difficulties to deal with multiple constraints. Therefore, the density method has grown more popular in the topology optimization community. This paper follows this trend, and is organized as follows.

The methodologies for the topology optimization of magnetic and electric field descriptions are presented in §2a,c, with sensitivity analysis, presented in §2b,d. The numerical implementations that solve the corresponding variational problem are presented in §2e. Several test problems are presented in §3 to demonstrate the feasibility and robustness of the combined method. In the expose, all the mathematical descriptions are formulated in a Cartesian coordinate system, and we consider only non-magnetic materials.

2. Methodology

This section develops, sequentially, a magnetic field-centric, as well as an electric field-centric formulation. Our approach is to first determine the governing equations, then to formulate the optimization problem statement, as well as its associated sensitivity analysis, after which we present the solution process. As an overview, we have made the following choices for the methodology:

- the density method is used to implement material interpolation functions, and is selected for its robustness;
- the continuous adjoint method is used to perform the sensitivity analysis;
- the Helmholtz equation-based density filter and threshold projection is used to regularize the topology optimization problem and ensure convergence;
- the edge element-based finite-element method is used to solve the electromagnetic field and enforce the divergence-free condition; and
- the topology optimization method is developed for electromagnetic waves, respectively, based on the magnetic and the electric fields as independent variables.

(a) Magnetic field formulation

As is well known, the Maxwell equations are widely used to describe propagating electromagnetic phenomena. Under a time harmonic assumption, they can be reduced to stationary equations that can be solved. For example, by setting the time-dependent factor to be $e^{j\omega t}$, the magnetic field wave equation can be derived as

$$\left.\begin{aligned} &\nabla \times [\epsilon_r^{-1} \nabla \times (\mathbf{H}_s + \mathbf{H}_i)] - k_0^2 \mu_r (\mathbf{H}_s + \mathbf{H}_i) = \mathbf{0}, \quad \text{in } \Omega \\ \text{and} \quad &\nabla \cdot \mathbf{H}_s = 0, \quad \text{in } \Omega \end{aligned}\right\} \tag{2.1}$$

where the scattered-field formulation is used with the magnetic field $\mathbf{H}$ split into two parts, i.e. the incident wave $\mathbf{H}_i$ and scattered field $\mathbf{H}_s$; the second equation is the divergence-free condition of the scattered field; the incident wave is the wave propagating in free space, and it satisfies the divergence-free condition $\nabla \cdot \mathbf{H}_\mathrm{i} = 0$; ϵ_r and μ_r are respectively the relative permittivity and permeability of the propagation medium; ω is the angular frequency; t is the time; $j = \sqrt{-1}$ is the imaginary unit; $k_0 = \omega\sqrt{\epsilon_0\mu_0}$ is the free space wavenumber, with ϵ_0 and μ_0, respectively, representing the free space permittivity and permeability; $\varOmega \subset \mathbb{R}^3$ is the computational domain. To truncate the electromagnetic field towards infinite space and investigate the field in a given space without artefacts, boundary conditions need to be imposed on the border $\partial\varOmega \subset \mathbb{R}^2$ of the computational domain $\varOmega$. The boundary conditions for equation (2.1) usually include a first-order adsorbing condition, as well as perfect magnetic and electric conditions. The first-order absorbing condition is usually used to truncate the field distribution at infinity [47]

$$\mathbf{n} \times (\epsilon_\mathrm{r}^{-1}\nabla \times \mathbf{H}_\mathrm{s}) - jk_0\sqrt{\epsilon_\mathrm{r}^{-1}\mu_\mathrm{r}}\mathbf{n} \times (\mathbf{H}_\mathrm{s} \times \mathbf{n}) = \mathbf{0}, \quad \text{on } \varGamma_\mathrm{a} \tag{2.2}$$

where $\mathbf{n}$ is the unit outward normal vector at the trace $\partial\varOmega$; $\varGamma_\mathrm{a} \subset \partial\varOmega$ is the absorbing boundary. The perfect magnetic and electric conditions are used to describe the truncation of the field at perfect magnetic and electric conductors, where the tangential continuity of the field is ensured

$$\left.\begin{aligned} &\mathbf{n} \times (\mathbf{H}_\mathrm{s} + \mathbf{H}_\mathrm{i}) = \mathbf{0}, \quad \text{on } \varGamma_\mathrm{PMC} \\ \text{and} \quad &\mathbf{n} \times [\epsilon_\mathrm{r}^{-1}\nabla \times (\mathbf{H}_\mathrm{s} + \mathbf{H}_\mathrm{i})] = \mathbf{0}, \quad \text{on } \varGamma_\mathrm{PEC} \end{aligned}\right\} \tag{2.3}$$

where $\varGamma_\mathrm{PMC}$ and $\varGamma_\mathrm{PEC}$ are the perfect magnetic and electric boundaries, respectively. The perfect magnetic boundary condition can also be used to express the symmetry of the field.

Topology optimization requires material interpolation between different material phases, in which the spatial distribution of relative permittivity needs to be determined. The relative permittivity is interpolated by a design variable that represents the structural topology. In this research, the design variable is filtered by a Helmholtz filter [50,51] to ensure the robust evolution of the design variable and remove tiny structures with sizes close to that of the discretized elements. The Helmholtz filter is implemented by solving the following Helmholtz equation

$$\left.\begin{aligned} &-r^2\nabla \cdot \nabla\gamma_\mathrm{f} + \gamma_\mathrm{f} = \gamma, \quad \text{in } \varOmega \\ \text{and} \quad &\mathbf{n} \cdot \nabla\gamma_\mathrm{f} = 0, \quad \text{on } \partial\varOmega \end{aligned}\right\} \tag{2.4}$$

where r is the filter radius chosen based on numerical experiments [51]; γ_f is the filtered design variable; $\gamma \in L^2(\varOmega)$, satisfying $0 \le \gamma \le 1$, is the design variable. To remove the 'grey' region in the obtained structural topology, the filtered design variable is projected by the threshold method [52–54]

$$\gamma_\mathrm{fp} = \frac{\tanh(\beta\xi) + \tanh(\beta(\gamma_\mathrm{f} - \xi))}{\tanh(\beta\xi) + \tanh(\beta(1 - \xi))} \tag{2.5}$$

where γ_fp, the projected design variable, is the physical density taking the place of the design variable to represent the structural topology [54]; $\xi \in [0, 1]$ and β are the threshold and projection parameters, respectively; for the choice of the values of ξ and β, the reader is referred to [51,55]. After filtering and projection, the relative permittivity is interpolated by the physical density instead of the design variable. The interpolation is implemented between two different materials, respectively, corresponding to the cases $\gamma_\mathrm{fp} = 0$ and $\gamma_\mathrm{fp} = 1$; the material interpolation can be chosen to be the linear form [20]

$$\epsilon_\mathrm{r} = \epsilon_{r1} + \gamma_\mathrm{fp}(\epsilon_{r2} - \epsilon_{r1}), \tag{2.6}$$

where ϵ_{r1} and ϵ_{r2} are the relative permittivities of the two materials.

Based on the above description, the variational problem for the topology optimization of magnetic field described three-dimensional electromagnetic waves can be formulated to be

$$\text{find } \gamma \text{ to maximize or minimize} \quad J(\mathbf{H}_\mathrm{s}, \nabla\times\mathbf{H}_\mathrm{s}, \gamma_\mathrm{fp}; \gamma)$$
$$\text{subject to} \quad \begin{cases} \nabla\times[\epsilon_\mathrm{r}^{-1}\nabla\times(\mathbf{H}_\mathrm{s}+\mathbf{H}_\mathrm{i})] - k_0^2\mu_\mathrm{r}(\mathbf{H}_\mathrm{s}+\mathbf{H}_\mathrm{i}) = \mathbf{0}, & \text{in } \Omega \\ \nabla\cdot\mathbf{H}_\mathrm{s} = 0, \quad \text{in } \Omega \\ -r^2\nabla\cdot\nabla\gamma_\mathrm{f} + \gamma_\mathrm{f} = \gamma, \quad \text{in } \Omega \\ 0 \le \gamma \le 1, \end{cases} \tag{2.7}$$

where the Helmholtz filter equation is included in the partial differential equation constraints. J is the generally formulated cost functional, which includes both the domain and boundary integrations of the unknown state variables

$$J(\mathbf{H}_\mathrm{s}, \nabla\times\mathbf{H}_\mathrm{s}, \gamma_\mathrm{fp}; \gamma) = \int_\Omega A(\mathbf{H}_\mathrm{s}, \nabla\times\mathbf{H}_\mathrm{s}, \gamma_\mathrm{fp}; \gamma)\,\mathrm{d}\Omega + \int_{\Gamma_\mathrm{a}\bigcup\Gamma_\mathrm{PEC}} B(\mathbf{H}_\mathrm{s})\,\mathrm{d}\Gamma, \tag{2.8}$$

where A and B are integral functionals chosen based on a mathematical description of the desired electromagnetic wave behaviour.

(b) Magnetic field sensitivity analysis

In this section, the variational problem in equation (2.7) is analysed to derive the gradient information used to evolve the design variable. It has been clarified that the adjoint method is an efficient approach with which to derive the gradient expressions of a partial differential equation (PDE) constrained optimization problem [56]. Being different from the conventional case, the functional space for the wave equation (2.1) needs to be chosen to satisfy the divergence-free condition [46]

$$\mathcal{V}_\mathbf{H} \doteq \{\mathbf{u}\in\mathcal{H}(\mathrm{curl};\Omega)\,|\,\nabla\cdot\mathbf{u}=0, \text{ in } \Omega;\ \mathbf{n}\times\mathbf{u}=\mathbf{0}, \text{ on } \Gamma_\mathrm{PMC}\}, \tag{2.9}$$

where

$$\mathcal{H}(\mathrm{curl};\Omega) = \{\mathbf{u}\in(L^2(\Omega))^3\,|\,\nabla\times\mathbf{u}\in(L^2(\Omega))^3\} \tag{2.10}$$

and $L^2(\Omega)$ is the second-order Lebesgue integrable functional space. Then, according to the Kurash–Kuhn–Tucker condition of the PDE constrained optimization problem [56], the adjoint equations of the wave equation and Helmholtz filter can be obtained as: find $\mathbf{H}_\mathrm{sa}\in\mathcal{V}_\mathbf{H}$ and $\gamma_\mathrm{fa}\in\mathcal{H}^1(\Omega)$, satisfying

$$\begin{aligned} &\int_\Omega \frac{\partial A}{\partial\mathbf{H}_\mathrm{s}}\cdot\boldsymbol{\phi} + \frac{\partial A}{\partial\nabla\times\mathbf{H}_\mathrm{s}}\cdot(\nabla\times\boldsymbol{\phi}) + \epsilon_\mathrm{r}^{-1}(\nabla\times\bar{\mathbf{H}}_\mathrm{sa})\cdot(\nabla\times\boldsymbol{\phi}) - k_0^2\mu_\mathrm{r}\bar{\mathbf{H}}_\mathrm{sa}\cdot\boldsymbol{\phi}\,\mathrm{d}\Omega \\ &+\int_{\Gamma_\mathrm{a}} jk_0\sqrt{\epsilon_\mathrm{r}^{-1}\mu_\mathrm{r}}(\mathbf{n}\times\bar{\mathbf{H}}_\mathrm{sa}\times\mathbf{n})\cdot(\mathbf{n}\times\boldsymbol{\phi}\times\mathbf{n}) + \frac{\partial B}{\partial\mathbf{H}_\mathrm{s}}\cdot\boldsymbol{\phi}\,\mathrm{d}\Gamma \\ &+\int_{\Gamma_\mathrm{PEC}} \frac{\partial B}{\partial\mathbf{H}_\mathrm{s}}\cdot\boldsymbol{\phi}\,\mathrm{d}\Gamma = 0,\ \forall\,\boldsymbol{\phi}\in\mathcal{V}_\mathbf{H} \end{aligned} \tag{2.11}$$

and

$$\begin{aligned} &\int_\Omega r^2\nabla\bar{\gamma}_\mathrm{fa}\cdot\nabla\phi + \bar{\gamma}_\mathrm{fa}\phi + \frac{\partial A}{\partial\gamma_\mathrm{f}}\phi + \frac{\partial\epsilon_\mathrm{r}^{-1}}{\partial\gamma_\mathrm{f}}[\nabla\times(\mathbf{H}_\mathrm{s}+\mathbf{H}_\mathrm{i})]\cdot(\nabla\times\bar{\mathbf{H}}_\mathrm{sa})\phi\,\mathrm{d}\Omega \\ &+\int_{\Gamma_\mathrm{a}}\left[jk_0\frac{\partial\sqrt{\epsilon_\mathrm{r}^{-1}\mu_\mathrm{r}}}{\partial\gamma_\mathrm{f}}\mathbf{n}\times(\mathbf{H}_\mathrm{s}\times\mathbf{n}) + \mathbf{n}\times\left(\frac{\partial\epsilon_\mathrm{r}^{-1}}{\partial\gamma_\mathrm{f}}\nabla\times\mathbf{H}_\mathrm{i}\right)\right]\cdot(\mathbf{n}\times\bar{\mathbf{H}}_\mathrm{sa}\times\mathbf{n})\phi\,\mathrm{d}\Gamma \\ &+\int_{\Gamma_\mathrm{PEC}}\left[\mathbf{n}\times\left(\frac{\partial\epsilon_\mathrm{r}^{-1}}{\partial\gamma_\mathrm{f}}\nabla\times\mathbf{H}_\mathrm{i}\right)\right]\cdot(\mathbf{n}\times\bar{\mathbf{H}}_\mathrm{sa}\times\mathbf{n})\phi\,\mathrm{d}\Gamma = 0, \quad \forall\,\phi\in\mathcal{H}^1(\Omega), \end{aligned} \tag{2.12}$$

where $\mathbf{H}_{sa}$ and γ_{fa} are the adjoint variables of $\mathbf{H}_s$ and γ_f, respectively; $\mathcal{H}^1(\Omega)$ is the first-order Sobolev space; the overbar represents the conjugate operation of a complex variable. Furthermore, the adjoint derivative of the cost functional can be derived as

$$\delta J = \int_\Omega Re\left(\frac{\partial A}{\partial \gamma} - \bar{\gamma}_{fa}\right)\delta\gamma\,\mathrm{d}\Omega. \tag{2.13}$$

where *Re* is the operator used to extract the real part of a complex function.

(c) Electric field formulation

In electromagnetics, electric field-based descriptions are preferred when the electromagnetic performance is evaluated based on values of the electric field. In this case, the Maxwell equations can be reduced into the electric field-based wave equation

$$\left.\begin{aligned} &\nabla\times[\mu_r^{-1}\nabla\times(\mathbf{E}_s+\mathbf{E}_i)] - k_0^2\epsilon_r(\mathbf{E}_s+\mathbf{E}_i) = \mathbf{0}, \quad \text{in } \Omega\\ \text{and}\quad &\nabla\cdot[\epsilon_r(\mathbf{E}_s+\mathbf{E}_i)] = 0, \quad \text{in } \Omega \end{aligned}\right\} \tag{2.14}$$

where the scattered-field formulation is also used with the electric field $\mathbf{E}$ split into two parts, i.e. the incident wave $\mathbf{E}_i$ and scattered field $\mathbf{E}_s$; the second equation is the divergence-free condition of the electric displacement; the incident wave is the wave propagating in free space, satisfying the divergence-free condition $\nabla\cdot\mathbf{E}_i = 0$. The boundary conditions for equation (2.14) also usually include a first-order adsorbing condition, and perfect magnetic and electric conditions, which are respectively expressed as

$$\left.\begin{aligned} &\mathbf{n}\times(\mu_r^{-1}\nabla\times\mathbf{E}_s) - jk_0\sqrt{\mu_r^{-1}\epsilon_r}\mathbf{n}\times(\mathbf{E}_s\times\mathbf{n}) = \mathbf{0}, \quad \text{on } \Gamma_a\\ &\mathbf{n}\times[\mu_r^{-1}\nabla\times(\mathbf{E}_s+\mathbf{E}_i)] = \mathbf{0}, \quad \text{on } \Gamma_{PMC}\\ \text{and}\quad &\mathbf{n}\times(\mathbf{E}_s+\mathbf{E}_i) = \mathbf{0}, \quad \text{on } \Gamma_{PEC}. \end{aligned}\right\} \tag{2.15}$$

Being different from the magnetic field-based description case presented in §2a, the divergence-free condition in equation (2.14) must consider the gradient of the relative permittivity, because the permittivity gradient always arises in the topology optimization procedure. The permittivity gradient could result in the inapplicability of numerical solution methods, e.g. edge element-based finite-element method, which can otherwise fulfil the divergence-free condition of the field in piecewise homogeneous media [47]. To circumvent this problem, the computational domain Ω is assumed to be piecewise homogeneous. Under the assumption of piecewise homogeneity, the relative permittivity is a constant distribution in every piecewise domain, i.e.

$$\epsilon_r(\Omega_n) = \text{const}, \quad n = 1, 2\ldots N, \tag{2.16}$$

where Ω_n is a homogeneous piece of the computational domain, satisfying

$$\Omega = \bigcup_{n=1}^{N}\Omega_n;\ \Omega_p\bigcap\Omega_q = \varnothing,\ \text{with } p\neq q, \quad \text{and} \quad p, q = 1, 2\ldots N, \tag{2.17}$$

where N is the number of homogeneous pieces included in the computational domain. Based on the assumed piecewise homogeneity, the divergence-free condition in equation (2.14) can be transformed into

$$\nabla\cdot\mathbf{E}_s = 0, \quad \text{in } \Omega. \tag{2.18}$$

The applicability of an edge element-based finite-element method is thereby ensured. Corresponding to the assumption of piecewise homogeneity, an element-wise topology optimization method should be developed for electric field described electromagnetic waves, because the structural topology will be obtained as a combination of several homogeneous pieces of material.

To avoid the low efficiency and high computational cost convolution filter [54] usually used in element-wise topology optimization, the following regularization procedure is proposed that transforms the continuously defined design variable into a piecewise material density, and furthermore, to implement material interpolation, where the applicability of the Helmholtz filter is ensured for the design variable:

(i) define the continuous design variable γ in Ω;
(ii) filter the design variable using a Helmholtz filter (equation (2.4)); and
(iii) transfer the filtered design variable γ_f into a piecewise version

$$\gamma^\mathrm{e} = \sum_{n=1}^{N} \gamma_n^\mathrm{e}(\Omega) \tag{2.19}$$

with

$$\gamma_n^\mathrm{e}(\Omega) = \begin{cases} \dfrac{1}{V_{\Omega_n}} \int_{\Omega_n} \gamma_\mathrm{f} \, \mathrm{d}\Omega, & \forall \mathbf{x} \in \Omega_n \\ 0, & \forall \mathbf{x} \in \Omega \backslash \Omega_n \end{cases} \tag{2.20}$$

where V_{Ω_n} is the volume of Ω_n;
(iv) project the piecewise design variable γ^e into the material density $\gamma_\mathrm{p}^\mathrm{e}$

$$\gamma_\mathrm{p}^\mathrm{e}(\gamma^\mathrm{e}) = \frac{\tanh(\beta\xi) + \tanh(\beta(\gamma^\mathrm{e} - \xi))}{\tanh(\beta\xi) + \tanh(\beta(1-\xi))}; \tag{2.21}$$

(v) implement material interpolation with the material density $\gamma_\mathrm{p}^\mathrm{e}$, which represents the material distribution in the derived structural topology

$$\epsilon_\mathrm{r} = \epsilon_{r1} + \gamma_\mathrm{p}^\mathrm{e}(\epsilon_{r2} - \epsilon_{r1}), \tag{2.22}$$

where ϵ_{r1} and ϵ_{r2} are the relative permittivities of the two materials.

Based on the above regularization procedure, element-wise topology optimization can be implemented with a continuously defined design variable. Subsequently, the variational problem for the topology optimization of the electric field described three-dimensional electromagnetic waves can be formulated as

$$\begin{aligned} &\text{find } \gamma \text{ to maximize or minimize} \quad J(\mathbf{E}_\mathrm{s}, \nabla \times \mathbf{E}_\mathrm{s}, \gamma_\mathrm{p}^\mathrm{e}; \gamma) \\ &\text{subject to} \quad \begin{cases} \nabla \times [\mu_\mathrm{r}^{-1} \nabla \times (\mathbf{E}_\mathrm{s} + \mathbf{E}_\mathrm{i})] - k_0^2 \epsilon_\mathrm{r} (\mathbf{E}_\mathrm{s} + \mathbf{E}_\mathrm{i}) = \mathbf{0}, & \text{in } \Omega \\ \nabla \cdot \mathbf{E}_\mathrm{s} = 0, & \text{in } \Omega \\ -r^2 \nabla \cdot \nabla \gamma_\mathrm{f} + \gamma_\mathrm{f} = \gamma, & \text{in } \Omega, \\ 0 \le \gamma \le 1 \end{cases} \end{aligned} \tag{2.23}$$

where Ω is the piecewise homogeneous computational domain; J is a generally formulated cost functional

$$J(\mathbf{E}_\mathrm{s}, \nabla \times \mathbf{E}_\mathrm{s}, \gamma_\mathrm{p}^\mathrm{e}; \gamma) = \int_\Omega A(\mathbf{E}_\mathrm{s}, \nabla \times \mathbf{E}_\mathrm{s}, \gamma_\mathrm{p}^\mathrm{e}; \gamma) \, \mathrm{d}\Omega + \int_{\Gamma_\mathrm{a} \bigcup \Gamma_\mathrm{PMC}} B(\mathbf{E}_\mathrm{s}) \, \mathrm{d}\Gamma, \tag{2.24}$$

where A and B are again integral functionals chosen based on a mathematical description of the desired electromagnetic wave behaviour.

(d) Electric field sensitivity analysis

The Lagrangian multiplier-based adjoint sensitivity analysis of the variational problem in equation (2.23) is implemented as follows. The functional space and trace operators of equation

(2.14) are similarly defined as that in §2b, except that

$$\mathcal{V}_{\mathrm{E}} \doteq \{\mathbf{u} \in \mathcal{H}(\mathrm{curl}; \Omega) \mid \nabla \cdot \mathbf{u} = 0, \text{ in } \Omega; \ \mathbf{n} \times \mathbf{u} = \mathbf{0}, \text{ on } \Gamma_{\mathrm{PEC}}\}. \tag{2.25}$$

Then, according to the Kurash–Kuhn–Tucker condition of the PDE constrained optimization problem [56], the adjoint equations can be obtained as: find $\mathbf{E}_{\mathrm{sa}} \in \mathcal{V}_{\mathrm{E}}$ and γ_{fa} in $\mathcal{H}^1(\Omega)$, satisfying

$$\begin{aligned}
&\int_{\Omega} \frac{\partial A}{\partial \mathbf{E}_{\mathrm{s}}} \cdot \boldsymbol{\phi} + \frac{\partial A}{\partial \nabla \times \mathbf{E}_{\mathrm{s}}} \cdot (\nabla \times \boldsymbol{\phi}) + \mu_{\mathrm{r}}^{-1} (\nabla \times \bar{\mathbf{E}}_{\mathrm{sa}}) \cdot (\nabla \times \boldsymbol{\phi}) - k_0^2 \epsilon_{\mathrm{r}} \bar{\mathbf{E}}_{\mathrm{sa}} \cdot \boldsymbol{\phi} \, \mathrm{d}\Omega \\
&\quad + \int_{\Gamma_{\mathrm{a}}} jk_0 \sqrt{\epsilon_{\mathrm{r}} \mu_{\mathrm{r}}^{-1}} (\mathbf{n} \times \bar{\mathbf{E}}_{\mathrm{sa}} \times \mathbf{n}) \cdot (\mathbf{n} \times \boldsymbol{\phi} \times \mathbf{n}) + \frac{\partial B}{\partial \mathbf{E}_{\mathrm{s}}} \cdot \boldsymbol{\phi} \, \mathrm{d}\Gamma \\
&\quad + \int_{\Gamma_{\mathrm{PMC}}} \frac{\partial B}{\partial \mathbf{E}_{\mathrm{s}}} \cdot \boldsymbol{\phi} \, \mathrm{d}\Gamma = 0, \quad \forall \boldsymbol{\phi} \in \mathcal{V}_{\mathrm{E}}
\end{aligned} \tag{2.26}$$

and

$$\int_{\Omega} r^2 \nabla \bar{\gamma}_{\mathrm{fa}} \cdot \nabla \phi + \bar{\gamma}_{\mathrm{fa}} \phi + A_{\gamma^{\mathrm{e}}} \phi - S_{\gamma^{\mathrm{e}}} \phi \, \mathrm{d}\Omega = 0, \quad \forall \phi \in \mathcal{H}^1(\Omega), \tag{2.27}$$

where $\mathbf{E}_{\mathrm{sa}}$ and γ_{fa} are the adjoint variables of $\mathbf{E}_{\mathrm{s}}$ and γ_{f}, respectively; $A_{\gamma^{\mathrm{e}}}(\Omega)$ is defined to be

$$A_{\gamma^{\mathrm{e}}} = \sum_{n=1}^{N} A_{\gamma_n^{\mathrm{e}}}(\Omega_n), \quad \text{with } A_{\gamma_n^{\mathrm{e}}}(\Omega_n) = \begin{cases} \dfrac{1}{V_{\Omega_n}} \displaystyle\int_{\Omega_n} \frac{\partial A}{\partial \gamma_{\mathrm{p}}^{\mathrm{e}}} \frac{\partial \gamma_{\mathrm{p}}^{\mathrm{e}}}{\partial \gamma^{\mathrm{e}}} \, \mathrm{d}\Omega, & \forall \mathbf{x} \in \Omega_n \\ 0, & \forall \mathbf{x} \in \Omega \backslash \Omega_n. \end{cases} \tag{2.28}$$

and $S_{\gamma^{\mathrm{e}}}(\Omega)$ is defined to be

$$S_{\gamma^{\mathrm{e}}} = \sum_{n=1}^{N} S_{\gamma_n^{\mathrm{e}}}(\Omega_n), \quad \text{with } S_{\gamma_n^{\mathrm{e}}}(\Omega_n) = \begin{cases} \dfrac{1}{V_{\Omega_n}} \displaystyle\int_{\Omega_n} k_0^2 \frac{\partial \epsilon_{\mathrm{r}}}{\partial \gamma_{\mathrm{p}}^{\mathrm{e}}} \frac{\partial \gamma_{\mathrm{p}}^{\mathrm{e}}}{\partial \gamma^{\mathrm{e}}} (\mathbf{E}_{\mathrm{s}} + \mathbf{E}_{\mathrm{i}}) \cdot \bar{\mathbf{E}}_{\mathrm{sa}} \, \mathrm{d}\Omega, & \forall \mathbf{x} \in \Omega_n \\ 0, & \forall \mathbf{x} \in \Omega \backslash \Omega_n. \end{cases} \tag{2.29}$$

The adjoint derivative of the cost functional can be derived as

$$\delta J = \int_{\Omega} Re \left(\frac{\partial A}{\partial \gamma} - \bar{\gamma}_{\mathrm{fa}} \right) \delta \gamma \, \mathrm{d}\Omega. \tag{2.30}$$

(e) Solving

In the wave equations and corresponding adjoint equations, a divergence-free condition needs to be satisfied for both the state variable and the adjoint variable. Therefore, the edge element-based finite-element method is used to solve the wave equations and adjoint equations, where brick elements are used to discretize the computational domain and simultaneously ensure the divergence-free condition [47]. For the Helmholtz filter, the filter equation (2.4) and its adjoint equation are solved using the standard Galerkin finite-element method.

The topology optimization method for three-dimensional electromagnetic waves is implemented by a gradient-based iterative procedure, where the gradient information is derived by sensitivity analysis as demonstrated in §2b,d respectively, corresponding to the variational problems in equation (2.7) and (2.23). The flowcharts for iteratively solving the variational problems (equations (2.7) and (2.23), respectively) corresponding to the magnetic field formulation and electric field formulation are shown in figure 1*a*,*b*. The iterative procedure includes the following steps: (i) solve the wave equations with the current design variable; (ii) solve the adjoint equations based on the solution of the wave equations; (iii) compute the adjoint derivative of the design objective; and (iv) update the design variable using the method of moving asymptotes (MMA) [57]. During the solving procedure, the filter radius r of the Helmholtz filter in equation (2.4) is set to be the size of the finite elements used to discretize the computational domain; the threshold parameter ξ in equation (2.5) and (2.21) is set to be 0.5; the initial value of the projection parameter β is set to be 1 and it is doubled after every fixed number of iterations until the preset maximal value 1024 is reached (11 cycles). The above-mentioned steps

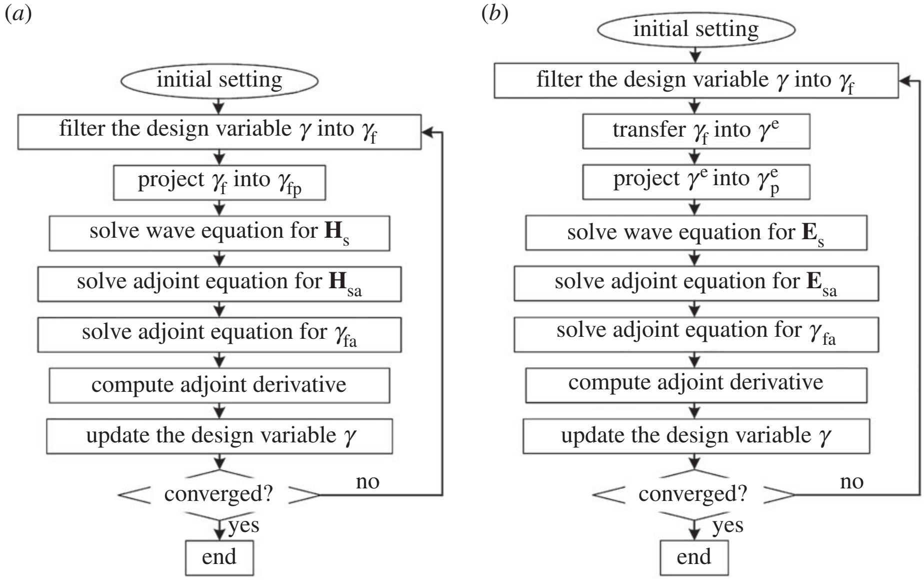

Figure 1. Flowcharts for the iterative solution of topology optimization problems for three-dimensional electromagnetic waves. (*a*) Flowchart for the iterative solution of variational problem 2.7 and (*b*) flowchart for the iterative solution of variational problem 2.23.

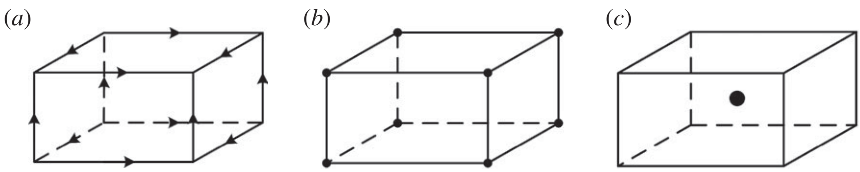

Figure 2. The finite-elements used in the topology optimization procedure. (*a*) Linear edge element for $\mathbf{H}_s$ or $\mathbf{E}_s$, (*b*) linear nodal element for γ and γ_f and (*c*) zeroth-order discontinuous element for γ^e.

are implemented iteratively until the stopping criterion is satisfied, specified to be the change of the objective values in five consecutive iterations satisfying

$$\frac{1}{5}\sum_{i=1}^{4}\frac{|J_{k-i}-J_{k-i-1}|}{|J_k|}\leq\varepsilon,\quad \beta\geq 1024 \tag{2.31}$$

in the kth iteration, where J_k is the objective value computed in the kth iteration; ε is the tolerance chosen to be 1×10^{-3}. Because the iteration number is set to be 40 before doubling the projection parameter, the maximal iterative number is set to be 440 in this paper.

All of the finite-element method-based numerical solutions and integrations are carried out in the commercial software COMSOL MULTIPHYSICS (v. 3.5; http://www.comsol.com), where all numerical implementation are based on the software's basic module: *Comsol Multiphysics* → *PDE Modes* → *PDE, Weak Form*. For details on the setting of the *PDE Modes* and numerical integrations, one can refer to (http://www.comsol.com) [58,59].

In the optimization procedure for magnetic field described electromagnetic waves, the magnetic field is interpolated using linear edge elements (figure 2*a*); the design variable and filtered design variable is interpolated using linear nodal element (figure 2*b*). In the optimization procedure for electric field described electromagnetic waves, the electric field is interpolated using linear edge elements (figure 2*a*); the design variable and filtered design variable is interpolated using linear nodal elements (figure 2*b*); the filtered design variable is converted to piecewise form by interpolating the piecewise design variable using zeroth-order discontinuous elements (figure 2*c*), where Ω_n in equation (2.20) is set to be the space taken up by the brick elements. All the computations were performed on a Dell workstation (Dell Precision T5500, two Intel Xeon Quad X5550 CPUs with frequency 2.66 GHz, RAM 48 GB).

3. Numerical examples

To demonstrate the robustness of the developed topology optimization methods for three-dimensional electromagnetic waves, several numerical examples are presented as follows. The numerical examples include the topology optimization-based computational design of cloaks, resonators and splitters, which in turn demonstrate *min*-type, *max*-type and *max–min*-type optimization problems. The material used in all the numerical examples is a dielectric with relative permittivity equal to 2.

(a) Cloak

In this section, an electromagnetic cloak is computationally designed using the developed method. This is a typical *min*-type optimization problem. Topology optimization-based computational design of two-dimensional electromagnetic cloaks have been investigated for TM and TE incident waves, where two-dimensional is the reduced case with an infinite extension assumed in the third dimension [20–22]. Three-dimensional design is more flexible and practical for the consideration of realistic situations. In the following, electromagnetic cloaks are designed for a spherical perfect conductor. To cloak the sphere, the scattered field should be minimized to achieve phase matching of the total field around the conductor. The computational domain of the cloak is set to be a cube with side length equal to seven times the incident wavelength, as shown in figure 3*a*, where the cloak domain is set to be a spherical shell with external and internal radii equal to 2.5 and 0.75 times the incident wavelength, and the cloaked conductor is enclosed in a central spherical domain with a radius equal to 0.75 times the incident wavelength. The computational domain is discretized by $63 \times 63 \times 63$ brick elements.

For a magnetic field described electromagnetic cloak, the objective in equation (2.8) is set to be the normalized square norm of the scattered magnetic field

$$\min J = \frac{1}{J_0} \int_{\Omega_o} \mathbf{H}_s \cdot \bar{\mathbf{H}}_s \, d\Omega, \tag{3.1}$$

where Ω_o is the domain outside the spherical shell-shaped design domain; J_0 is the square norm of the uncloaked scattered magnetic field in the outside domain of the cloak. The obtained cloak topology, found by solving the corresponding topology optimization problem, is shown in figure 3*b*, with incident wave, uncloaked field, and cloaked field shown in figure 3*d*,*e*,*f*, where the incident wave is set to be the uniform plane wave $\mathbf{H}_i = (0, 0, e^{-jk_0x})$ with $k_0 = 20\pi$ rad m^{-1}. For an electric field described electromagnetic cloak, the objective in equation (2.24) is set to be the normalized square norm of the scattered electric field

$$\min J = \frac{1}{J_0} \int_{\Omega_o} \mathbf{E}_s \cdot \bar{\mathbf{E}}_s \, d\Omega, \tag{3.2}$$

where J_0 is the square norm of the uncloaked scattered electric field in the outside domain of the cloak. The obtained cloak topology, found by solving the corresponding topology optimization problem, is shown in figure 4*a*, with incident wave, uncloaked field and cloaked field, respectively, shown in figure 4*c*,*d*,*e*, where the incident wave is set to be the uniform plane wave $\mathbf{E}_i = (0, 0, e^{-jk_0x})$ with $k_0 = 20\pi$ rad m^{-1}. Objective convergent histories for both these two cases were, respectively, plotted in figures 3*c* and 4*b*, which has demonstrated the robustness of the convergent process of the solving procedure.

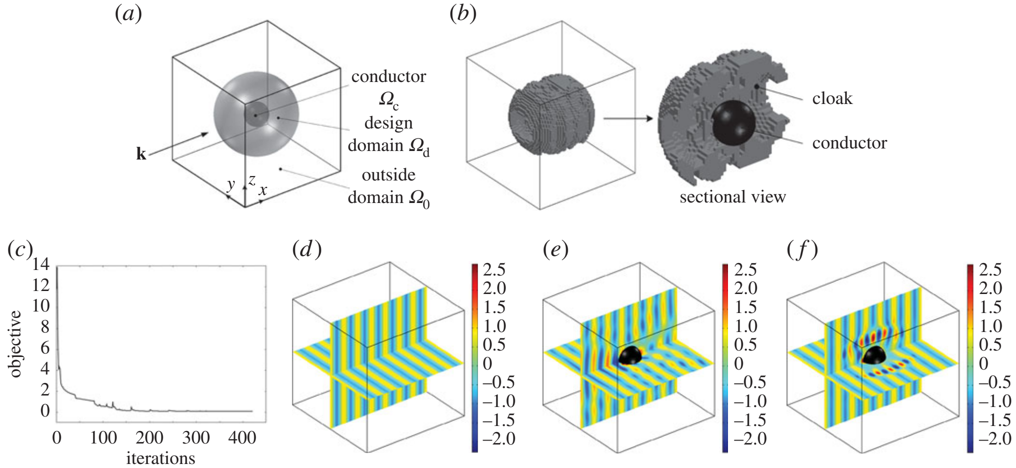

Figure 3. (*a*) Sketch of the computational domain for the topology optimization of electromagnetic cloaks, where **k** is the wavevector of the incident wave, Ω_c is the central spherical domain filled with a perfect conductor, Ω_d is the spherical shell-shaped design domain for the cloaks and Ω_0 is the domain outside of the design domain. The domains Ω_c and Ω_d are implicitly expressed by specifying spherical radius less than the given values for the convenience of discretizing the whole computational domain with brick elements. (*b*) Cloak topology derived using the developed topology optimization method for magnetic field described electromagnetic waves; (*c*) convergence history of the objective values during the solution procedure; (*d*) magnetic field of the uniform plane incident wave; (*e*) magnetic field distribution around the uncloaked spherical conductor; (*f*) magnetic field distribution around the cloaked spherical conductor. The CPU time cost is 129.27 h. (Online version in colour.)

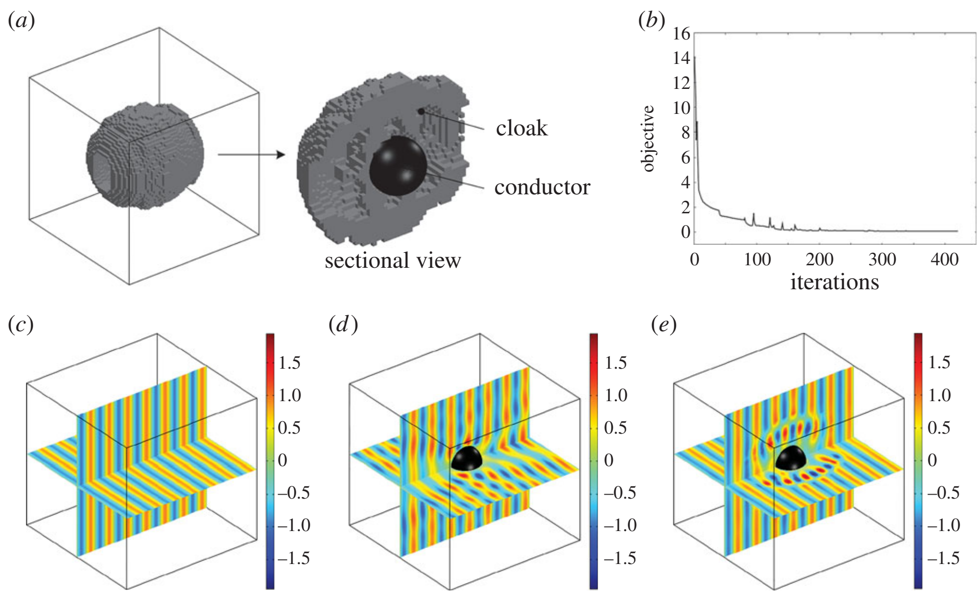

Figure 4. (*a*) Cloak topology derived using the developed topology optimization method for electric field described electromagnetic waves; (*b*) convergence history of the objective values during the solution procedure; (*c*) electric field of the uniform plane incident wave; (*d*) electric field distribution around the uncloaked spherical conductor; (*e*) electric field distribution around the cloaked spherical conductor. The CPU time cost is 119.69 h. (Online version in colour.)

The computationally designed cloaks have effectively reduced the scattered energy in the outside domain of the cloaks, and this can be confirmed by comparing the uncloaked and cloaked fields shown in figures 3*e*,*f* and 4*d*,*e*. For magnetic field-based design, the scattered energy is

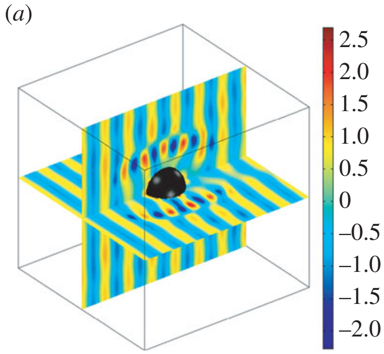

Figure 5. (*a*) Magnetic field distribution around the cloak in figure 4*a* induced by the incident wave in figure 3*d*; (*b*) electric field distribution around the cloak in figure 3*b* induced by the incident wave in figure 4*c*. (Online version in colour.)

Table 1. List of the objective values corresponding to figures 3*f* and 5*a*, 4*e* and 5*b*. The values corresponding to figures 3*f* and 5*a* are computed using equation (3.1); and the values corresponding to figures 4*e* and 5*b* are computed using equation (3.2).

figure 3*f*	figure 5*a*	figure 4*e*	figure 5*b*
0.061	0.786	0.076	1.364

weakened to be 0.061-fold of that of the uncloaked case; and it is weakened to be 0.076-fold of that of the uncloaked case, for electric field-based design. The field distributions shown in figures 3*f* and 4*e* demonstrate that phase matching is achieved for the propagating waves around the conductor. Therefore, cloaking of the conductor is realized for the case of a uniform incident plane wave, with the cloak computationally designed using a simple isotropic dielectric, a material class which is readily available in nature.

To confirm the optimality of the derived cloak topologies in figures 3*b* and 4*a*, the cross comparison is implemented by computing the scattered fields of these two cloak topologies with exchanging their corresponding incident waves. The magnetic field distribution around the cloak in figure 4*a* induced by the incident wave in figure 3*d* is shown in figure 5*a*; and electric field distribution around the cloak in figure 3*b* induced by the incident wave in figure 4*c* is shown in figure 5*b*. The objective values corresponding to figures 3*f* and 5*a*, 4*e* and 5*b* are listed in table 1. From the comparison of the values in table 1, the optimality can be confirmed for the derived cloak topologies in figures 3*b* and 4*a*.

(b) Dielectric resonator

This section considers *max*-type optimization problems, for which dielectric-based electromagnetic resonator design is a typical task. Electromagnetic resonators are designed to concentrate the electromagnetic energy in a specified spherical domain, where the total field should be maximized, hence achieving a resonance of the total field in this domain. The computational domain of the resonator is set to be a cube with side length equal to 2.5 times the incident wavelength, as shown in figure 6*a*, where the design domain is set to be a spherical shell with external and internal radii, respectively, equal to 1 and 0.3 times the incident wavelength, and the resonating domain is the central spherical domain with radius equal to 0.3 times the incident wavelength. The computational domain is discretized by $50 \times 50 \times 50$ brick elements.

For the magnetic field described case, the objective in equation (2.8) is set to be the normalized square norm of the total magnetic field in the resonating domain

$$\max J = \frac{1}{J_0} \int_{\Omega_r} \mathbf{H} \cdot \bar{\mathbf{H}} \, \mathrm{d}\Omega \tag{3.3}$$

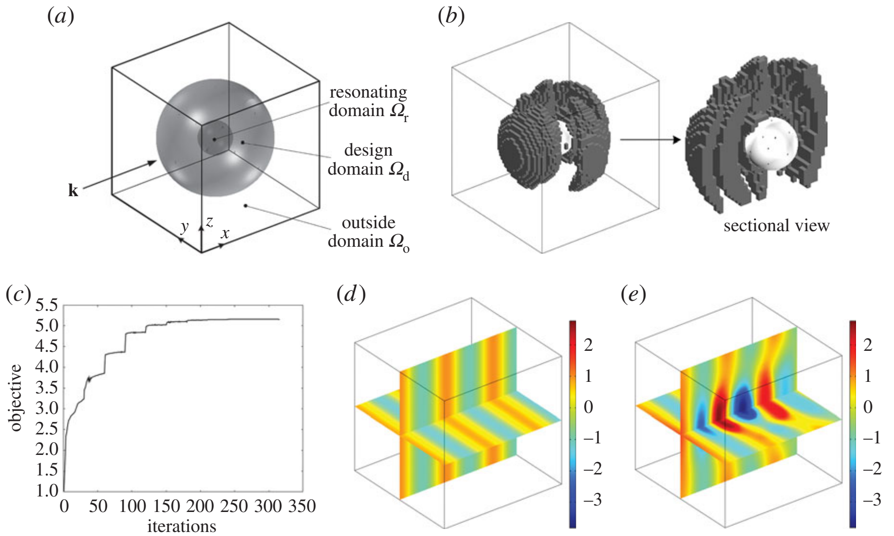

Figure 6. (*a*) Sketch of the computational domain for the topology optimization of electromagnetic resonators, where **k** is the wavevector of the incident wave, the central spherical domain Ω_r is the resonating domain with vacuum, Ω_d is the spherical shell-shaped design domain for the dielectric resonator, and Ω_o is the domain outside of the design domain. The domains Ω_r and Ω_d are implicitly expressed by specifying spherical radius less than the given values for the convenience of discretizing the whole computational domain with brick elements. (*b*) Resonator topology derived using the developed topology optimization method for magnetic field described electromagnetic waves; (*c*) convergence history of the objective values during the solution procedure; (*d*) magnetic field of the parallel plane incident wave; (*e*) magnetic field distribution around the magnetic resonator. The CPU time cost is 21.59 h. (Online version in colour.)

where Ω_r is the resonating domain; J_0 is the square norm of the total magnetic field in the resonating domain, with dielectric filled in the design domain. After implementing the solution procedure introduced in §2e, the obtained resonator topology is shown in figure 6*b*, with incident wave and resonating field shown in figure 6*d*,*e*, and in which the incident field is set to be the uniform plane wave $\mathbf{H}_i = (0, 0, e^{-jk_0x})$ with $k_0 = 20\pi$ rad m^{-1}. For the electric field described case, the objective in equation (2.24) is set to be the normalized square norm of the total electric field in the resonating domain

$$\max J = \frac{1}{J_0} \int_{\Omega_r} \mathbf{E} \cdot \bar{\mathbf{E}} \, d\Omega, \tag{3.4}$$

where J_0 is the square norm of the electric field in the resonating domain, with dielectric filled in the design domain. The obtained resonator topology is shown in figure 7*a*, with incident wave and resonating field, respectively, shown in figure 7*c*,*d*, where the incident wave is set to be the uniform plane wave $\mathbf{E}_i = (0, 0, e^{-jk_0x})$ with $k_0 = 20\pi$ rad m^{-1}. The objective convergent histories for both cases are plotted in figures 6*c* and 7*b*, and demonstrate the robustness of the convergence process of the solution procedure. The computationally designed resonators have effectively focused the electromagnetic energy in the resonating domain of the resonator, where the electromagnetic field has been enhanced effectively; and this can be confirmed by inspecting the field distribution shown in figures 6*e* and 7*d*.

To check the optimality of the derived resonator topologies in figures 6*b* and 7*a*, the similar cross comparison method is adopted as that in §3a. By exchanging the corresponding incident waves, the magnetic field distribution around the resonator in figure 7*a* induced by the incident wave in figure 6*d* is shown in figure 8*a*; and electric field distribution around the resonator in figure 6*b* induced by the incident wave in figure 7*c* is shown in figure 8*b*. The objective values corresponding to figures 6*e* and 8*a*, 7*d* and 8*b* are listed in table 2. From the comparison of the

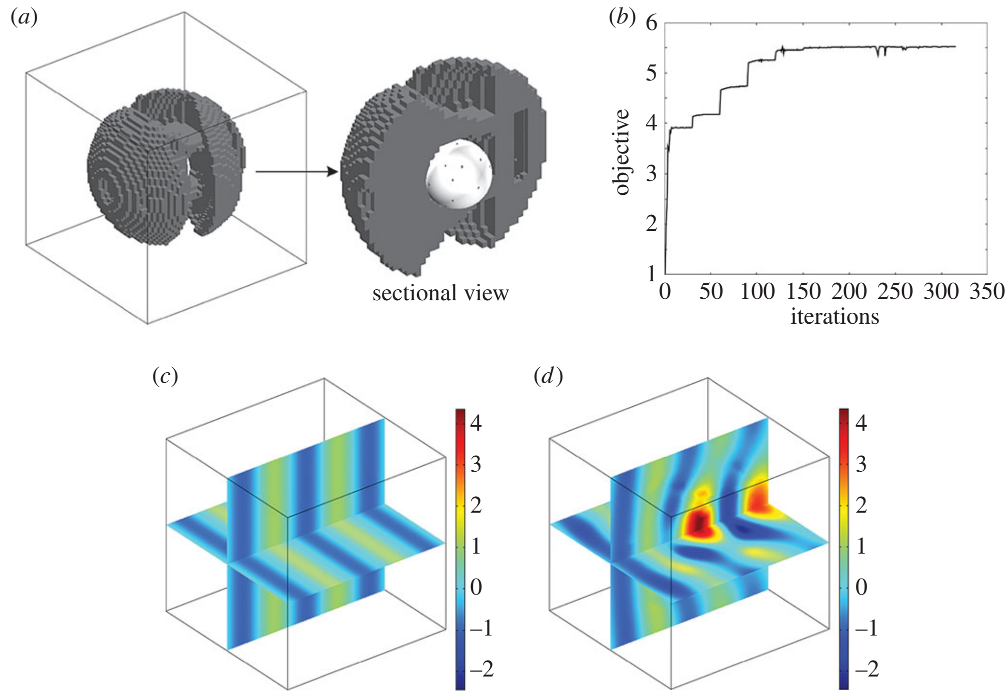

Figure 7. (*a*) Resonator topology derived using the developed topology optimization method for electric field described electromagnetic waves; (*b*) convergence history of the objective values during the solution procedure; (*c*) electric field of the parallel plane incident wave; (*d*) electric field distribution around the electric resonator. The CPU time cost is 22.36 h. (Online version in colour.)

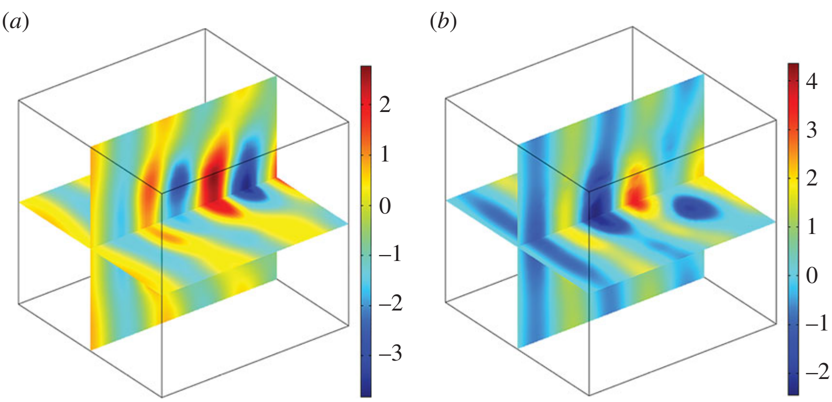

Figure 8. (*a*) Magnetic field distribution around the resonator in figure 7*a* induced by the incident wave in figure 6*d*; (*b*) electric field distribution around the resonator in figure 6*b* induced by the incident wave in figure 7*c*. (Online version in colour.)

values in table 2, the optimality can be confirmed for the derived resonator topologies in figures 6*b* and 7*a*.

(c) Dielectric beam splitter

An electromagnetic splitter is topologically optimized in the following, in order to demonstrate the robustness of the developed method when applied to *max–min*-type optimization problems.

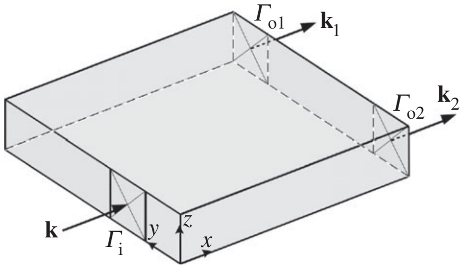

Figure 9. Sketch of the computational domain for the topology optimization of an electromagnetic splitter, where $\mathbf{k}$ is the incident wavevector at the incident boundary Γ_i, $\mathbf{k}_1$ and $\mathbf{k}_2$ are the parallel wavevectors of the output waves at the outlets Γ_{o1} and Γ_{o2}, Ω is the brick-shaped design domain.

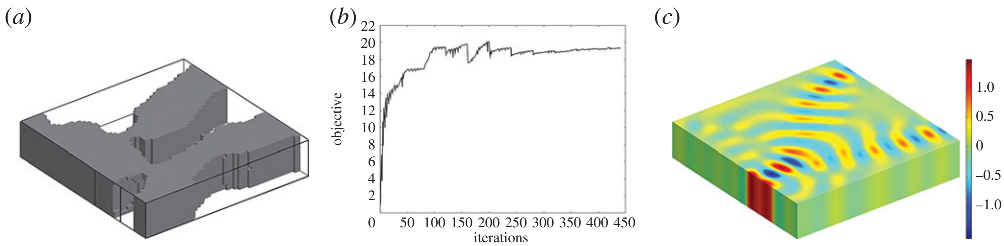

Figure 10. (*a*) Splitter topology derived using the developed topology optimization method for magnetic field described electromagnetic waves; (*b*) convergence history of the objective values during the solution procedure, where the objective values are normalized by the objective value corresponding to the case with the design domain uniformly filled by the chosen dielectric; (*c*) magnetic field distribution in the derived splitter. The CPU time cost is 25.96 h. (Online version in colour.)

Table 2. List of the objective values corresponding to figures 6*e* and 8*a*, 7*d* and 8*b*. The values corresponding to figures 6*e* and 8*a* are computed using equation (3.3); and the values corresponding to figures 7*d* and 8*b* are computed using equation (3.4).

figure 6*e*	figure 8*a*	figure 7*d*	figure 8*b*
5.151	2.106	5.524	2.975

For computationally designing the splitters, the computational domain is set up as shown in figure 9, where the electromagnetic energy enters the domain from the inlet Γ_i and output from the two specified outlets Γ_{o1} and Γ_{o2}. The computational domain is discretized by $60 \times 60 \times 12$ elements. The incident wave is set to be the z-polarized uniform plane wave with a frequency equal to 1×10^9 Hz.

The design objective of the splitter is to achieve equal and maximized energy levels at the two outlets. Therefore, for the magnetic field case, the design objective is set to be

$$\max \min \left\{ \int_{\Gamma_{o1}} \frac{1}{2}\mu_0\mu_r \mathbf{H} \cdot \bar{\mathbf{H}}\, \mathrm{d}\Gamma, \int_{\Gamma_{o2}} \frac{1}{2}\mu_0\mu_r \mathbf{H} \cdot \bar{\mathbf{H}}\, \mathrm{d}\Gamma \right\} \tag{3.5}$$

and for the electric field case, the design objective is modified to be

$$\max \min \left\{ \int_{\Gamma_{o1}} \frac{1}{2}\epsilon_0\epsilon_r \mathbf{E} \cdot \bar{\mathbf{E}}\, \mathrm{d}\Gamma, \int_{\Gamma_{o2}} \frac{1}{2}\epsilon_0\epsilon_r \mathbf{E} \cdot \bar{\mathbf{E}}\, \mathrm{d}\Gamma \right\}. \tag{3.6}$$

The splitter topology is derived as shown in figures 10 and 11, where the convergence histories of objective values and field distribution are included. From the field distribution in figures 10*c* and 11*c*, one can confirm by inspection the wave splitting performance of the computationally

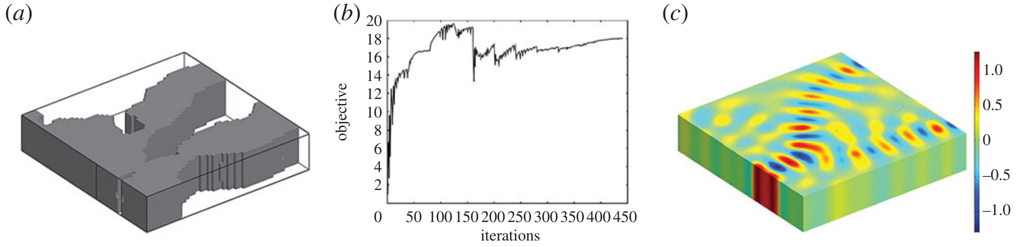

Figure 11. (*a*) Splitter topology derived using the developed topology optimization method for electric field described electromagnetic waves; (*b*) convergence history of the objective values during the solution procedure, where the objective values are normalized by the objective value corresponding to the case with the design domain uniformly filled by the chosen dielectric; (*c*) electric field distribution in the derived splitter. The CPU time cost is 11.08 h. (Online version in colour.)

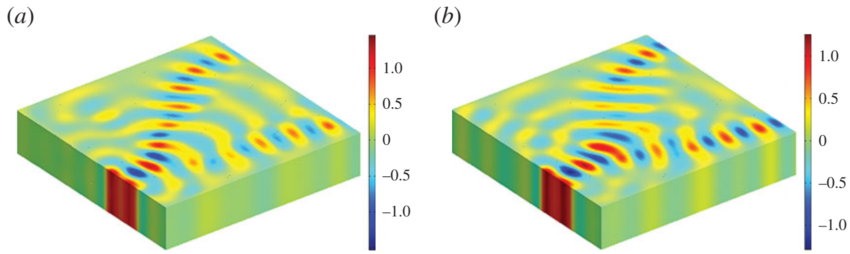

Figure 12. (*a*) Magnetic field distribution in the splitter in figure 11*a*, when it is used for the magnetic field; (*b*) electric field distribution in the splitter in figure 10*a*, when it is used for the electric field. (Online version in colour.)

Table 3. List of the objective values corresponding to figures 10*c* and 12*a*, 11*c* and 12*b*. The values corresponding to figures 10*c* and 12*a* are computed using equation (3.5); and the values corresponding to figures 11*c* and 12*b* are computed using equation (3.6).

figure 10*c*	figure 12*a*	figure 11*c*	figure 12*b*
0.034	0.025	0.032	0.026

designed splitters. The splitting and parallelization was achieved in approximately eight wavelengths for both versions.

The optimality of the derived splitter topologies in figures 10*a* and 11*a* is checked with the cross comparison implemented by exchanging the corresponding incident waves. When the splitter in figure 11*a* is used for the magnetic wave, the magnetic field is distributed as shown in figure 12*a*; and when the splitter in figure 10*a* is used for the electric field, the electric field is distributed as shown in figure 12*b*. The objective values corresponding to figures 10*c* and 12*a*, 11*c* and 12*b* are listed in table 3. From the comparison of the values in table 3, the optimality for the derived splitter topologies in figures 10*a* and 11*a* is confirmed.

4. Conclusion

This paper developed the topology optimization for three-dimensional electromagnetic waves based on an edge finite-element method. This choice of elements allowed the topology optimization procedures to inherently enforce divergence-free conditions for the magnetic and electric fields. The continuous adjoint method was used to carry out the sensitivity analysis of the topology optimization problems. In combination, a unified approach was developed for the topology optimization of three-dimensional structures interacting with electromagnetic waves.

A novel regularization procedure was developed, under the assumption of piecewise homogeneity of the computational domain. This procedure frees up the choice of methodology by providing a consistent method with which to express nodal data as element-based data for the design variables. The low efficiency and hence high computational cost convolution filter that is otherwise widely used in element-wise topology optimization is thereby avoided.

With the developed topology optimization method, the physical complexity of three-dimensional electromagnetic waves are properly treated during the inverse design of electromagnetic structures. As an outlook, the solution procedure is ready to be applied to the inverse design of practical three-dimensional electromagnetic structures, e.g. cloacking devices, resonators and waveguides, with feasibility demonstrated by the numerical examples.

Data accessibility. This article is solely based on numerical modelling and therefore has no data associated with it.
Competing interests. We have no competing interests.
Funding. We gratefully acknowledge the Deutsche Forschungsgemeinschaft (DFG) for funding Y.D. via the grant Metacoils. Y.D. also gratefully acknowledges the National Natural Scientific Funding of China for funding via the grant no. 51405465. J.G.K. gratefully acknowledges the European Research Council (ERC) for funding via the advanced grant no. 290586 (NMCEL).
Acknowledgements. The authors are grateful to Prof. K. Svanberg for supplying the MMA codes, and the reviewers' kind attention and valuable suggestions.
Disclaimer. Y.D. and J.G.K. conceived and designed the computational method; Y.D. carried out the computational code writing and numerical experiments; Y.D. and J.G.K. carried out results analysis, drafted and wrote the manuscript. Both authors gave final approval for publication.

References

1. Valentine J, Li J, Zentgraf T, Bartal G, Zhang X. 2009 An optical cloak made of dielectrics. *Nat. Mater.* **8**, 568–571. (doi:10.1038/nmat2461)
2. Alù A, Engheta N. 2009 Cloaking a sensor. *Phys. Rev. Lett.* **102**, 233901. (doi:10.1103/PhysRevLett.102.233901)
3. Liu Y, Zentgraf T, Bartal G, Zhang X. 2010 Transformational plasmon optics. *Nano Lett.* **10**, 1991–1997. (doi:10.1021/nl1008019)
4. Shin D, Urzhumov Y, Jung Y, Kang G, Baek S, Choi M, Park H, Kim K, Smith DR. 2012 Broadband electromagnetic cloaking with smart metamaterials. *Nat. Commun.* **3**, 1213. (doi:10.1038/ncomms2219)
5. Zentgraf T, Liu Y, Mikkelsen MH, Valentine J, Zhang X. 2011 Plasmonic Luneburg and Eaton lenses. *Nat. Nanotechnol.* **6**, 151–155. (doi:10.1038/nnano.2010.282)
6. Novotny L, Hulst N. 2011 Antennas for light. *Nat. Photon.* **5**, 83–90. (doi:10.1038/nphoton.2010.237)
7. Petryayeva E, Krull UJ. 2011 Localized surface plasmon resonance: Nanostructures, bioassays and biosensing—A review. *Anal. Chim. Acta* **706**, 8–24. (doi:10.1016/j.aca.2011.08.020)
8. Ebbesen TW, Lezec HJ, Ghaemi HF, Thio T, Wolff PA. 1998 Extraordinary optical transmission through sub-wavelength hole arrays. *Nature* **391**, 667–669. (doi:10.1038/35570)
9. Smith DR, Pendry JB, Wiltshire MCK. 2004 Metamaterials and negative refractive index. *Science* **35**, 788–792. (doi:10.1126/science.1096796)
10. Holloway CL, Kuester EF, Baker-Jarvis J, Kabos P. 2003 A double negative (DNG) composite medium composed of magnetodielectric spherical particles embedded in a matrix. *IEEE Trans. Antennas Propagat.* **51**, 2596–2603. (doi:10.1109/TAP.2003.817563)
11. Zheludev NI. 2010 The road ahead for metamaterials. *Science* **328**, 582–583. (doi:10.1126/science.1186756)
12. Yao K, Liu Y. 2014 Plasmonic metamaterials. *Nanotechnol. Rev.* **3**, 177–210. (doi:10.1166/rnn.2014.1051)
13. Kildishev AV, Boltasseva A, Shalaev VM. 2013 Planar photonics with metasurfaces. *Science* **339**, 1232009. (doi:10.1126/science.1232009)
14. Yu N, Capasso F. 2014 Flat optics with designer metasurfaces. *Nat. Mater.* **13**, 139–150. (doi:10.1038/nmat3839)
15. Joannopoulos JD, Johnson SG, Winn JN, Meade RD. 2008 *Photonic crystals: molding the flow of light*. Princeton, NJ: Princeton University Press.

16. Sigmund O, Hougaard KG. 2008 Geometric properties of optimal photonic crystals. *Phys. Rev. Lett.* **100**, 153904. (doi:10.1103/PhysRevLett.100.153904)
17. Frandsen LH, Elesin Y, Frellsen LF, Mitrovic M, Ding Y, Sigmund O, Yvind K. 2014 Topology optimized mode conversion in a photonic crystal waveguide fabricated in silicon-on-insulator material. *Opt. Express.* **22**, 8525–8532. (doi:10.1364/OE.22.008525)
18. Piggott AY, Lu J, Lagoudakis KG, Petykiewicz J, Babinec TM, Vučović J. 2015 Inverse design and demonstration of a compact and broadband on-chip wavelength demultiplexer. *Nat. Photon.* **9**, 374–377. (doi:10.1038/nphoton.2015.69)
19. Shen B, Wang P, Polson R, Menon R. 2015 An integrated-nanophotonics polarization beamsplitter with $2.4 \times 2.4\,\mu m^2$ footprint. *Nat. Photon.* **9**, 378–382. (doi:10.1038/nphoton.2015.80)
20. Andkjær J, Sigmund O. 2011 Topology optimized low-contrast all-dielectric optical cloak. *Appl. Phys. Lett.* **98**, 021112. (doi:10.1063/1.3540687)
21. Andkjær J, Mortensen NA, Sigmund O. 2012 Towards all-dielectric, polarization-independent optical cloaks. *Appl. Phys. Lett.* **100**, 101106. (doi:10.1063/1.3691835)
22. Fujii G, Watanabe H, Yamada T, Ueta T, Mizuno M. 2013 Level set based topology optimization for optical cloaks. *Appl. Phys. Lett.* **102**, 251106. (doi:10.1063/1.4812471)
23. Otomori M, Yamada T, Izui K, Nishiwaki S, Andkjær J. 2012 A topology optimization method based on the level set method for the design of negative permeability dielectric metamaterials. *Comput. Methods Appl. Mech. Eng.* **237–240**, 192–211. (doi:10.1016/j.cma.2012.04.022)
24. Diaz AR, Sigmund O. 2010 A topology optimization method for design of negative permeability metamaterials. *Struct. Multidisc. Optim.* **41**, 163–177. (doi:10.1007/s00158-009-0416-y)
25. Zhou S, Li W, Chen Y, Sun G, Li Q. 2011 Topology optimization for negative permeability metamaterials using level-set algorithm. *Acta Mater.* **59**, 2624–2636. (doi:10.1016/j.actamat.2010.12.049)
26. Andkjær J, Nishiwaki S, Nomura T, Sigmund O. 2010 Topology optimization of grating couplers for the efficient excitation of surface plasmons. *JOSA B* **27**, 1828–1832. (doi:10.1364/JOSAB.27.001828)
27. Zhou S, Li W, Li Q. 2010 Level-set based topology optimization for electromagnetic dipole antenna design. *J. Comput. Phys.* **229**, 6915–6930. (doi:10.1016/j.jcp.2010.05.030)
28. Feichtner T, Selig O, Kiunke M, Hecht B. 2012 Evolutionary optimization of optical antennas. *Phys. Rev. Lett.* **109**, 127701. (doi:10.1103/PhysRevLett.109.127701)
29. Hassan E, Wadbro E, Berggren M. 2014 Topology optimization of metallic antennas. *IEEE Trans. Antennas Propagat.* **62**, 2488–2500. (doi:10.1109/TAP.2014.2309112)
30. Deng Y, Liu Z, Song C, Wu J, Liu Y, Wu Y. 2015 Topology optimization-based computational design methodology for surface plasmon polaritons. *Plasmonics* **10**, 569–583. (doi:10.1007/s11468-014-9842-9)
31. Shim H, Ho VTT, Wang S, Tortorelli DA. 2009 Level set-based topology optimization for electromagnetic systems. *IEEE Trans. Magnet.* **45**, 1582–1585. (doi:10.1109/TMAG.2009.2012748)
32. Nomura T, Sato K, Taguchi K, Kashiwa T, Nishiwaki S. 2007 Structural topology optimization for the design of broadband dielectric resonator antennas using the finite difference time domain technique. *Int. J. Numer. Methods Eng.* **71**, 1261–1296. (doi:10.1002/nme.1974)
33. Duhring MB, Jensen JS, Sigmund O. 2008 Acoustic design by topology optimization. *J. Sound Vib.* **317**, 557–575. (doi:10.1016/j.jsv.2008.03.042)
34. Erentok A, Sigmund O. 2011 Topology optimization of sub-wavelength antennas. *IEEE Trans. Antennas Propagat.* **59**, 58–69. (doi:10.1109/TAP.2010.2090451)
35. Bendsøe M, Kikuchi N. 1988 Generating optimal topologies in optimal design using a homogenization method. *Comput. Methods Appl. Mech. Eng.* **71**, 197–224. (doi:10.1016/0045-7825(88)90086-2)
36. Rozvany GIN. 2001 Aims scope methods history and unified terminology of computer-aided optimization in structural mechanics. *Struct. Multidisc. Optim.* **21**, 90–108. (doi:10.1007/s001580050174)
37. Bendsøe M, Sigmund O. 2003 *Topology optimization-theory methods and applications*. Berlin, Germany: Springer.
38. Borrvall T, Petersson J. 2003 Topology optimization of fluid in Stokes flow. *Int. J. Numer. Methods Fluids* **41**, 77–107. (doi:10.1002/fld.426)

39. Gersborg-Hansen A, Bendsøe MP, Sigmund O. 2006 Topology optimization of heat conduction problems using the finite volume method. *Struct. Multidisc. Optim.* **31**, 251–259. (doi:10.1007/s00158-005-0584-3)
40. Akl W, El-Sabbagh A, Al-Mitani K, Baz A. 2008 Topology optimization of a plate coupled with acoustic cavity. *Int. J. Solids Struct.* **46**, 2060–2074. (doi:10.1016/j.ijsolstr.2008.05.034)
41. Kreissl S, Pingen G, Maute K. 2011 An explicit level-set approach for generalized shape optimization of fluids with the lattice Boltzmann method. *Int. J. Numer. Meth. Fluids* **65**, 496–519. (doi:10.1002/fld.2193)
42. Zhou S, Li Q. 2008 A variational level set method for the topology optimization of steady-state Navier–Stokes flow. *J. Comput. Phys.* **227**, 10 178–10 195. (doi:10.1016/j.jcp.2008.08.022)
43. Guest JK, Prevost JH. 2006 Topology optimization of creeping fluid flows using a Darcy–Stokes finite element. *Int. J. Numer. Methods Eng.* **66**, 461–484. (doi:10.1002/nme.1560)
44. Takezawa A, Haraguchi M, Okamoto T, Kitamura M. 2014 Cross-sectional optimization of whispering-gallery mode sensor with high electric field intensity in the detection domain. *IEEE. J. Sel. Top. Quant. Electron.* **20**, 1–10. (doi:10.1109/JSTQE.2014.2331651)
45. Takezawa A, Kitamura M. 2012 Cross-sectional shape optimization of whispering-gallery ring resonators. *IEEE/OSA J. Lightwave Tech.* **30**, 2776–2782. (doi:10.1109/JLT.2012.2207372)
46. Monk P. 2003 *Finite element methods for Maxwell's equations*. Oxford, UK: Oxford University Press.
47. Jin J. 2002 *The finite element method in electromagnetics*, 2nd edn. New York, NY: John Wiley & Sons.
48. Whitney H. 1957 *Geometric integration theory*. Princeton, NJ: Princeton University Press.
49. Nedelec JC. 1980 Mixed finite elements in R^3. *Numer. Methods* **35**, 315–341. (doi:10.1007/BF01396415)
50. Lazarov B, Sigmund O. 2011 Filters in topology optimization based on Helmholtz type differential equations. *Int. J. Numer. Methods Eng.* **86**, 765–781. (doi:10.1002/nme.3072)
51. Wang F, Lazarov BS, Sigmund O. 2011 On projection methods, convergence and robust formulations in topology optimization. *Struct. Multidiscip. Optim.* **43**, 767–784. (doi:10.1007/s00158-010-0602-y)
52. Xu S, Cai Y, Cheng G. 2010 Volume preserving nonlinear density filter based on Heaviside functions. *Struct. Multidiscip. Optim.* **41**, 495–505. (doi:10.1007/s00158-009-0452-7)
53. Guest J, Prevost J, Belytschko T. 2004 Achieving minimum length scale in topology optimization using nodal design variables and projection functions. *Int. J. Numer. Methods Eng.* **61**, 238–254. (doi:10.1002/nme.1064)
54. Sigmund O. 2007 Morphology-based black and white filters for topology optimization. *Struct. Multidiscip. Optim.* **33**, 401–424. (doi:10.1007/s00158-006-0087-x)
55. Kawamoto A, Matsumori T, Yamasaki S, Nomura T, Kondoh T, Nishiwaki S. 2011 Heaviside projection based topology optimization by a PDE-filtered scalar function. *Struct. Multidiscip. Optim.* **44**, 19–24. (doi:10.1007/s00158-010-0562-2)
56. Hinze M, Pinnau R, Ulbrich M, Ulbrich S. 2009 *Optimization with PDE constraints*. Berlin, Germany: Springer.
57. Svanberg K. 1987 The method of moving asymptotes: a new method for structural optimization. *Int. J. Numer. Meth. Eng.* **24**, 359–373. (doi:10.1002/nme.1620240207)
58. Deng Y, Liu Z, Zhang P, Liu Y, Wu Y. 2011 Topology optimization of unsteady incompressible Navier–Stokes flows. *J. Comput. Phys.* **230**, 6688–6708. (doi:10.1016/j.jcp.2011.05.004)
59. Olesen LB, Okkels F, Bruus H. 2006 A high-level programming language implementation of topology optimization applied to flow, steady-state Navier–Stokes. *Int. J. Numer. Meth. Eng.* **65**, 975–1001. (doi:10.1002/nme.1468)